

Capping the Electronic Lone Pair of the As(III) Central Atom in the Keggin-Type Anion: From Experimental–Theoretical Interplay to Evidence

Fa Ibrahima Bamba, Clément Falaise, Nathalie Leclerc, Mohamed Haouas,* Gildas Gbassi, Patrick Athéba, Mathieu Fregnaux, Jordi Buils, Mireia Segado-Centellas, Carles Bo,* and Emmanuel Cadot*



Cite This: <https://doi.org/10.1021/acs.inorgchem.5c00637>



Read Online

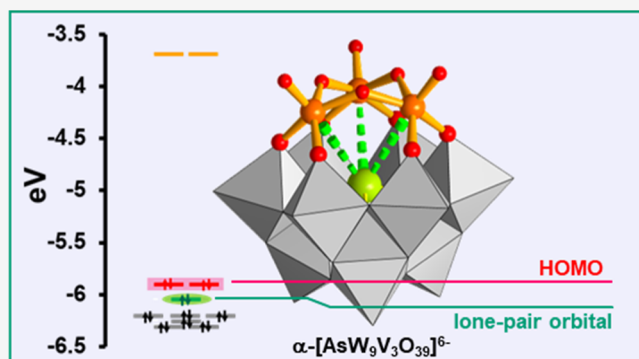
ACCESS |

Metrics & More

Article Recommendations

Supporting Information

ABSTRACT: The stereochemistry of the polycondensation processes within the Keggin-type derivatives is mainly governed by the nature of the assembly group X, being either tetrahedral or trigonal. Commonly, the use of trigonal units $\{XO_3\}$ gives rise to open molecular structures resulting from connections of $\{XM_9\}$ subunits through metal–oxo cationic fragments. Nevertheless, we show here that condensation of the vanadate VO_3^- onto the B-type isomer α -[As₉O₃₃]⁹⁻ led to the saturated mixed-metal Keggin derivative α -[As₉V₃O₃₉]⁶⁻. Experimental evidence was provided by multinuclear nuclear magnetic resonance (NMR) characterization, including ⁵¹V, ¹⁸³W, and ¹⁷O NMR, supported by XPS analysis revealing unambiguously the fingerprints of the As(III) atoms compared to those of As(V). Moreover, this unexpected structural feature is fully consistent with the versatile coordination of the V(V) atoms, which makes it possible for the μ_3 -O bridging oxygen of the $\{V_3\}$ cap to be absent in front of the electronic lone pair of the As(III) ion. In addition, DFT studies give consistency to the electronic structure of this new Keggin-type derivative. At last, structural, spectroscopic, and electrochemical properties of this new version of the Keggin structure were compared to other archetypal vanadium-containing anions and then discussed with regard to the geometry and vicinity of the vanadium atoms.



Downloaded via UNIV ROVIRA I VIRGILI on May 20, 2025 at 16:30:03 (UTC).

See https://pubs.acs.org/sharingguidelines for options on how to legitimately share published articles.

INTRODUCTION

Polyoxometalates (POMs) represent a remarkable class of polynuclear metal oxide anions built from early transition metal cations like V^V, Mo^{VI}, or W^{VI}.^{1,2} However, POM assemblies can include almost all the chemical elements in their metal–oxo framework that result from an extremely wide chemical composition associated with high structural diversity.³ Actually, one of the most striking properties of POM compounds is surely their ability to exchange electrons reversibly and massively without significant structural change,^{4,5} making them promising electroactive components for numerous applications in various domains in relationship with electrochemical energy conversion or storage.^{6,7}

However, these promising applications are linked to their intrinsic mixed-valence fundamental electronic properties, which essentially fall into three classes according to Robin & Day's classification.⁸ Then, depending on the structure, composition, or medium, various behaviors can be observed for the transferred d electrons such as (i) strongly localized (class I), thermally/optically delocalized (class II), or fully delocalized within metal-centered orbitals (class III). In

context, these properties give rise to many potential and specific applications where polyoxometalates are interfaced with various materials such as carbon-,^{9,10} nitride,¹¹ or sulfide¹²-based nanomaterials. Furthermore, the incorporation of transition metals into the POM framework corresponds to a practical and simple method for the design of robust mixed-metal molecular electrocatalysts, which operate from a fine electronic interplay between the transition metal catalytic site and the redox-active POM units.¹³ Then, such an approach has demonstrated to be fruitful to develop relevant POM-based electrocatalysts, efficient for different reactions such as proton,^{14,15} CO₂,¹⁶ O₂ or N₂ reduction,^{17,18} as well as water oxidation^{19,20} or biomass conversion.²¹ Another promising application of POM-based systems is their use as active

Received: February 11, 2025

Revised: April 26, 2025

Accepted: April 30, 2025

components in redox flow batteries. In particular, vanadium-containing POMs exhibit high redox potentials centered on the V^V/V^{IV} couple with values between ~0.5 and ~0.8 V vs Ag–AgCl, making them good candidates for catholyte matrices.²² Nevertheless, the redox properties of the V centers depend in part on the structural environment of the {VO_x} polyhedra.²³ As an illustrative example, the redox potential of the V center in the monosubstituted Dawson-type anion [P₂W₁₇VO₆₂]⁷⁻ is modified by about 60 mV when the location of the V atom changes from the polar (α_2 isomer) to the equatorial (α_1 isomer) position within the POM framework.²⁴ Herein, we report on the first Keggin-type anion that exhibits a triad of pure square-pyramidal vanadium(V) capping the trivacant B-[AsW₉O₃₃]⁹⁻ subunit. We provide ample evidence of such a molecular organization using diverse and complementary analytical methods such as X-ray diffraction; ⁵¹V, ¹⁸³W, and ¹⁷O nuclear magnetic resonance (NMR); XPS; electrochemistry; and theoretical calculations, all of which are consistent with or confirm the presence of the central trigonal {AsO₃} group in close contact with the {V₃O₆} cap in line with the structural hypothesis. In this study, the physicochemical consequences of oxygen deficiency of the Keggin framework have been evaluated by comparing spectroscopic and electrochemical properties with other archetypical vanadium-substituted polyoxotungstates such as the Keggin-type trisubstituted α -(1,2,3)-[AsW₉V₃O₄₀]⁶⁻ or the sandwich-type α -B-[AsW₉O₃₃)₂(VO)₃]⁹⁻ anions, where vanadium centers exhibit an octahedral or square-pyramidal environment, respectively.

RESULTS AND DISCUSSION

Synthesis. The development of polyoxotungstate chemistry has mapped comprehensive interconversion schemes that make possible the design of mixed-metal compounds using rational protocols, where stereospecific acidic condensation and basic hydrolysis processes alternate in multistep strategies.²⁵ For example, such a synthetic methodology has proven to be highly relevant for the synthesis of Mo–V–W Dawson-type anions, allowing the isolation of more than 20 derivatives, differing in their Mo/V/W composition and the location of the metallic centers that gives rise to numerous positional isomers.^{26,27} A similar methodology can also be applied to the polyoxotungstates deriving from the Keggin series. While successive addition of metalate ions on the A-type trivacant anions α -A-[PW₉O₃₄]⁹⁻ or α -A-[SiW₉O₃₄]¹⁰⁻ can restore the saturated Keggin-type anions α -(1,2,3)-[XW₉M₃O₄₀]ⁿ⁻, the use of the B-type isomers α -B-[XW₉O₃₃]⁹⁻ with X = As^{III}, Sb^{III}, or Bi^{III} in comparable conditions gives modular species such as dimeric or macrocyclic arrangements.^{28–31}

This stereochemical difference arises from the presence of the trigonal assembling group {XO₃}, whose electronic lone pair is expected to induce unfavorable electrostatic and steric repulsions with the μ_3 -oxygen atom (O_a-type) of the {M₃O₇} capping groups (see Figure 1). Then, the stereochemistry of the B-type α -[XW₉O₃₃]⁹⁻ is mostly known to produce sandwich-type compounds or large modular species resulting from connection of the B-[AsW₉O₃₃]⁹⁻ moiety through cationic metallic units.^{29,30} Actually, the restoration of the Keggin structure from the B-type anion might be possible in the case where μ_3 -O_a is absent, which means that the three metallic centers of the capping triad would adopt a square-pyramidal environment. Such a situation remains rare with tungsten(VI) or molybdenum(VI) but frequently observed

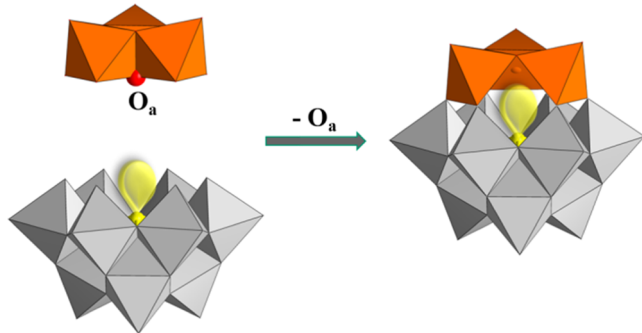


Figure 1. Schematic view of the formal restauration of the Keggin-type structure from the B-type α -[AsW₉O₃₃]⁹⁻ by the addition of a fourth triad {M₃O₆} containing a missing μ_3 -O_a oxygen atom.

with metal centers exhibiting lower oxidation state.^{32,33} In the case of vanadium(V), both situations are encountered depending on the steric environment of the coordination sphere of the vanadium atom.³⁴ Thus, condensation of vanadate ions [VO₃]⁻ on the trivacant species [AsW₉O₃₃]⁹⁻ has been investigated by using ⁵¹V NMR. For ratio V/[AsW₉] ~ 3, ⁵¹V NMR analysis reveals the presence of two predominant species observed at -509 ppm and -544 ppm which have been attributed to the Lindqvist anion³⁵ *cis*-[V₂W₄O₁₉]⁴⁻ and to the targeted species α -(1,4,9)-[AsW₉V₃O₃₉]⁶⁻, respectively. Actually, the balance between both species is sensitive to the pH. Whereas at pH ~ 1, the formation of the Lindqvist derivative is favored, in acetate buffer (pH = 4.8), the condensation reaction results mainly in the formation of the Keggin-type anion α -(1,4,9)-[AsW₉V₃O₃₉]⁶⁻ as the predominant species. Applying precipitation and crystallization usual procedures allows us to get K₆[α -(1,4,9)-AsW₉V₃O₃₉]⁶⁻·14H₂O with a purity close to 100%. Moreover, the conventional trivanadium-substituted K₆[α -(1,2,3)-AsW₉V₃O₄₀]⁶⁻·22H₂O anion has been prepared from the A-type trivacant anion α -A-[AsW₉O₃₄]⁹⁻ using procedure adapted from the literature^{25,36} (see Section S3 for synthesis details). Furthermore, the numbering of the positions of the three vanadium atoms in the Keggin-type arrangement follows the IUPAC recommendations (for details, see Section S2),³⁷ and a selection of arrangements resulting from condensation of vanadate on the A- or B-type trivacant {AsW₉} are depicted in Figure 2a–c.

Structural Analysis. The potassium salt K₆[α -(1,4,9)-AsW₉V₃O₃₉]⁶⁻·14H₂O gave crystals suitable for single-crystal X-ray diffraction analysis. Structure refinement has been carried out using the tetragonal system in the *P43m* space group (Section S4 for further details). The structure analysis reveals the presence of a Keggin-type anion in the cubic crystallographic cell in which the three vanadium and the nine tungsten atoms were not distinguishable among the location of the 12 metallic positions. Such a situation, shown in Figure 3a, is fairly consistent with a statistical disorder of the anion over its crystallographic position that results of 12 equivalent metallic positions occupied statistically by 25% of the vanadium atom and 75% of the tungsten atom. Furthermore, such a disorder generates a quite perfect central tetrahedron, which arises from the equal distribution of the central {AsO₃} group over the four equivalent positions of the tetrahedron. According to this disorder scheme, the three O_a-type oxygen atoms have been refined with a statistical occupancy factor of 75% over four tetrahedral positions. Then, despite the disorder that precludes

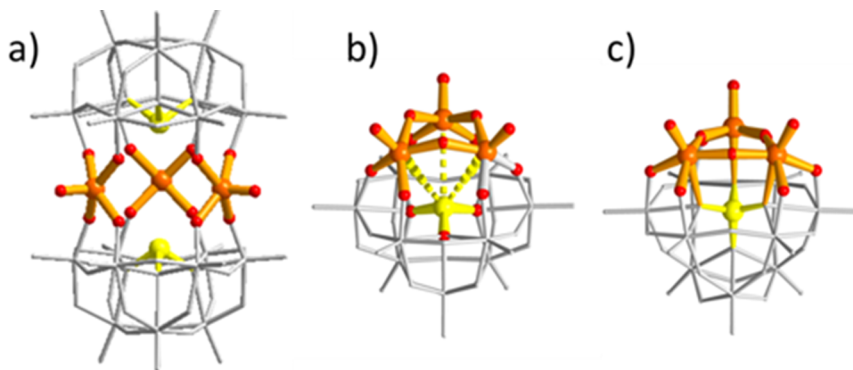
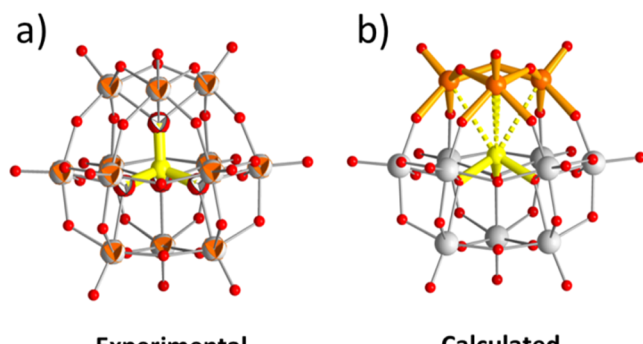


Figure 2. Structural representations highlighting different arrangements of the vanadium centers, including the square-based pyramidal within (a) the sandwich-type compound $\alpha\text{-B-[AsW}_9\text{O}_{33}\text{]}_2(\text{VO})_3\text{]}^{9-}$ and in (b) $\alpha\text{-(1,4,9)-[AsW}_9\text{V}_3\text{O}_{39}\text{]}^{6-}$ or octahedral in (c) $\alpha\text{-(1,2,3)-[AsW}_9\text{V}_3\text{O}_{40}\text{]}^{6-}$ (c); color code: orange spheres and sticks = vanadium atoms and V–O bonds, yellow spheres and sticks = arsenic atoms and As–O bonds, and gray sticks = W–O frameworks.



Experimental

Calculated

Figure 3. Ball and stick representations of the $\alpha\text{-(1,4,9)-[AsW}_9\text{V}_3\text{O}_{39}\text{]}^{6-}$ anion. (a) Experimental X-ray diffraction analysis showing a disordered situation where the $\{\text{V}_3\}$, $\{\text{W}_3\}$ triads and the $\{\text{AsO}_3\}$ trigonal group are distributed statistically over the four tetrahedral positions; (b) calculated structure showing the trivanadium cap closing the $[\text{AsW}_9\text{O}_{33}]$ unit and interacting with the electronic lone pair carried by the central As(III) atom. Color code: orange sphere = vanadium, gray sphere = tungsten, red = oxygen; yellow = arsenic; and the dotted yellow lines highlight the 3.32 Å separation distance between the square-pyramidal V atoms and the central As atom.

the location of the V and W atoms, the important result of this study lies in the evidence that condensation of vanadate ions onto the B-type trivacant anion $\alpha\text{-B-[AsW}_9\text{O}_{33}\text{]}^{9-}$ is able to restore the Keggin-type anions. Then, the structural analysis revealed bond lengths and angle parameters, which lie in the usual range found for the archetypical Keggin-type structure, such as the $[\alpha\text{-GaW}_{12}\text{O}_{40}\text{]}^{5-}$ anion, in which the central atom Ga(III) belongs to the same period of that of the As(III) atom (Section S5 and Table S2 for structural details).³⁸ Nevertheless, assuming that the central arsenic ion retains the As(III) oxidation state by carrying the electronic lone pair in the trigonal geometry, the environment of the three vanadium atoms in the metal–oxo shell of the Keggin-type framework remains questioning.

Computational studies have therefore been performed to circumvent the disorder situation by optimizing a geometry that consists of a $\alpha\text{-B-[AsW}_9\text{O}_{33}\text{]}$ subunit capped by three square-pyramidal vanadium atoms forming a triad (see Figure 3b). The calculated structure has been established in the C_{3v} symmetry, and orbital energies and Gibbs free energies indicate that such a structural arrangement should exhibit

similar stability to the conventional anion $\alpha\text{-(1,2,3)-[AsW}_9\text{V}_3\text{O}_{40}\text{]}^{6-}$. In the structure, the three square-pyramidal vanadium centers are equally separated by a distance of 3.324 Å from the As atom, while the calculated V=O bond distances exhibit a usual value of 1.624 Å. Besides, the W=O bond lengths remain significantly longer (1.744 Å).

These computed geometrical parameters have been compared to those obtained from the conventional Keggin-type anion $\alpha\text{-(1,4,9)-[AsW}_9\text{V}_3\text{O}_{40}\text{]}^{6-}$ or from the sandwich-type compound $\alpha\text{-B-[AsW}_9\text{O}_{33}\text{]}_2(\text{VO})_3\text{]}^{9-}$ highlighting slight but significant variations of the V=O bond length in relationship with the specific situation of the vanadium atoms (see Section S5 and Table S2). Then, the shortest V=O distance (1.589 (9) Å), however, is observed in the sandwich-type anion, where the V center retains a pure square-pyramidal arrangement.³⁴ The longest V=O distance is, however, observed in the conventional Keggin ion $\alpha\text{-[AsW}_9\text{V}_3\text{O}_{40}\text{]}^{6-}$ in which the vanadium centers maintain a classical octahedral geometrical environment by interacting with $\mu_3\text{-O}_a$ located trans to the V=O bond. Despite the long $\text{O}_a\cdots\text{V}$ distance of 2.455 Å, the trans-influence is manifested by a slight increase in the V=O bond length of 1.626 Å. At last, in the B-type Keggin anion, the vanadium atoms adopt an intermediate situation with a V=O bond distance of 1.624 Å, which could be the fingerprint of the trans-influence arising from the interaction between the electronic lone pair of the As atom and the V metal centers (see Figure 3b).

Spectroscopic Studies. Infrared Spectrum. The infrared spectrum of the B-type Keggin anion, shown in Figure 4, is typical of that of a conventional Keggin anion, showing main absorptions in the expected spectral ranges. Nevertheless, careful comparative examination of experimental data supported by calculations makes it possible to extract reliable trends related to the B-type Keggin structure. The $\{\text{M=O}\}$ vibrators give rise absorptions in the $950\text{--}1000\text{ cm}^{-1}$ region corresponding to either symmetric or antisymmetric stretching modes.^{39,40} The infrared spectrum of $\alpha\text{-(1,4,9)-[AsW}_9\text{V}_3\text{O}_{39}\text{]}^{6-}$ reveals a strong absorption band at 952 cm^{-1} and a higher energy one at 977 cm^{-1} of medium intensity. Such a situation appears more pronounced with the sandwich compound, which exhibits a strong band at 959 cm^{-1} and a medium one at 993 cm^{-1} . Nonetheless, in the conventional Keggin-type ion $\alpha\text{-(1,2,3)-[AsW}_9\text{V}_3\text{O}_{40}\text{]}^{6-}$, only a single quasi-symmetric absorption is observed at 958 cm^{-1} , probably due to the six-coordinated environment of the V

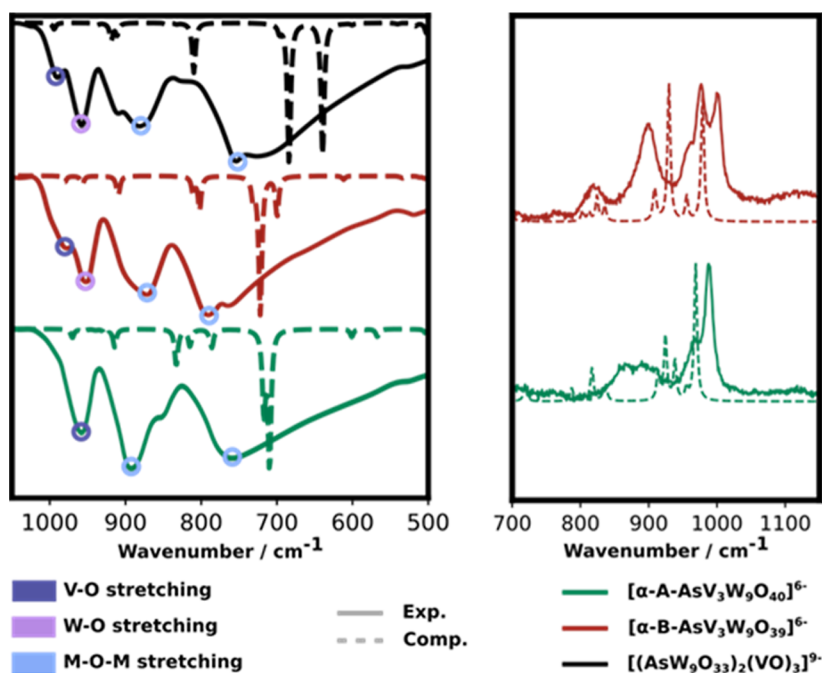


Figure 4. Left: experimental and calculated infrared spectra of Keggin-type anions $\alpha\text{-}(1,2,3)\text{-}[{\text{AsW}_9\text{V}_3\text{O}_{40}}]^{6-}$ (green) and $\alpha\text{-}(1,4,9)\text{-}[{\text{AsW}_9\text{V}_3\text{O}_{39}}]^{6-}$ (red) compared to that of the sandwich-type compound $[(\alpha\text{-B-AsW}_9\text{O}_{33})_2(\text{VO})_3]^{9-}$ (black). Superimposition of the three infrared spectra highlights significant differences in the region of the M=O stretching mode (ca. 1000 cm⁻¹), sensitive to the geometry of the V atom, octahedral in the A-type, and square-pyramidal in the B-type and sandwich-type spectra. Right: experimental and calculated Raman spectra of the $\alpha\text{-}(1,4,9)\text{-}[{\text{AsW}_9\text{V}_3\text{O}_{39}}]^{6-}$ (red line) and $\alpha\text{-}(1,2,3)\text{-}[{\text{AsW}_9\text{V}_3\text{O}_{40}}]^{6-}$ (green line) anions acquired in an aqueous solution.

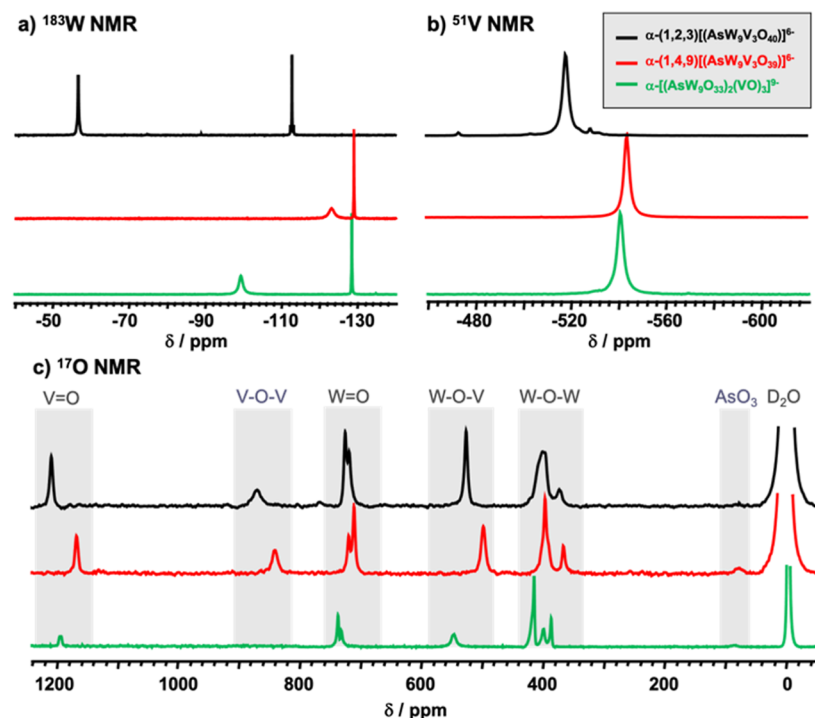


Figure 5. Multinuclear (a) ¹⁸³W, (b) ⁵¹V, and (c) natural abundance ¹⁷O NMR spectra of the $\alpha\text{-}(1,4,9)\text{-B-}[{\text{AsW}_9\text{V}_3\text{O}_{39}}]^{6-}$ anion in an aqueous solution at room temperature (in red) compared with those of the $\alpha\text{-}(1,2,3)\text{-A-}[{\text{AsW}_9\text{V}_3\text{O}_{40}}]^{6-}$ and $\alpha\text{-B-}[{\text{AsW}_9\text{O}_{33})_2(\text{VO})_3]^{9-}$ anions in black and green, respectively.

atoms that reduces the wavenumber of the $\nu(\text{V=O})$ stretching mode by the trans-influence of the $\mu_3\text{-Oa}$ atom leading to closer $\nu(\text{V=O})$ and $\nu(\text{W=O})$ absorptions. Furthermore, computational studies are rather consistent with these observations, showing that the $\nu(\text{V=O})$ modes are quite

sensitive to the environment of the V atom, increasing from 970 cm⁻¹ for octahedral to 994 cm⁻¹ for a square-pyramidal geometry (see Figure 4A and Section S6 and Table S3). Meanwhile, the remaining part of the infrared spectrum agrees with that of the Keggin-type ion showing absorptions

attributed to the stretching of the bridging modes M—O—M at 872 cm⁻¹ for the corner-shared junctions and at 747 and 794 cm⁻¹ for the edge-shared junctions. Furthermore, absorption related to the ν_{as} (As—O_a) mode is observed as a shoulder at 900 cm⁻¹. The calculated frequencies for the As—O vibration slightly differ from the experimental values. For the sandwich type, this vibration is located at 697 cm⁻¹. For the two different Keggin molecules, the values are also different. The B-type Keggin absorbs at 731 cm⁻¹ for the AsO₃ symmetrical stretching, while the conventional A-type Keggin has two absorptions at 833 and 828 cm⁻¹ for antisymmetrical and symmetrical stretching, respectively. In general, the computational IR spectrum is shifted to lower wavenumbers, keeping the relative positions of the peaks.

Raman Spectrum. The Raman spectrum of the α -(1,4,9)-B-[AsW₉V₃O₃₉]⁶⁻ anion in an aqueous solution (see Figure 4) nicely supports the analysis given for the infrared data. This Raman spectrum reveals two intense bands that should correspond to two symmetrical M=O_d breathing modes, attributed, respectively, to {V=O} vibrations at 1002 cm⁻¹ and {W=O_d} vibrations at 977 cm⁻¹. Conversely, the Raman spectrum of the α -(1,2,3)-[AsW₉V₃O₄₀]⁶⁻ anion contains only one intense band at 967 cm⁻¹, consistent with the overlapped {V=O} and {W=O} vibrations within the breathing M=O_d mode. In addition, the distribution of V centers in the Keggin structure also modifies the 900–800 cm⁻¹ region, which contains mainly antisymmetrical M—O—M vibrations, intense in the infrared and generally weak in the Raman mode.⁴⁰ Here, the presence of the three vanadium centers on the {1,4,9} sites gives rise to two distinct bands observed at 902 and 867 cm⁻¹, while the {1,2,3} derivative produces the usual weak, broad, and overlapped signal in the 900–800 cm⁻¹ range observed with the conventional Keggin-type anion. Again, the absence of V—O_a interactions should significantly strengthen the V—O_c—V junctions, with respect to the V—O—W and W—O—W junctions. This could explain the presence of these two absorptions attributed to both types of junctions. The calculated Raman spectrum also reveals the presence of two intense signals in the mentioned region. The signal for the A-type Keggin at around 930 cm⁻¹ represents several contributions from different absorptions, whereas they are differentiated in the experimental spectrum.

NMR (Liquid State in D₂O Solution). ⁵¹V, ¹⁸³W, and ¹⁷O NMR spectra of the α -(1,4,9)-B-[AsW₉V₃O₃₉]⁶⁻ anion and those of the two other POMs are shown in Figure 5a–c. Analysis of these spectra removes any ambiguity in the purity of the three compounds. The ⁵¹V NMR spectra contain a single resonance for each case, consistent with the expected symmetry that makes the three vanadium nuclei equivalent. Nonetheless, the ⁵¹V NMR chemical shift is quite sensitive to the environment of the V atom and could be influenced by its coordination number (CN) showing a systematic deshielding of the V nuclei as its coordination number increases from CN = 4–6.⁴¹ Such a trend is nicely satisfied with a close chemical shift for both the α -(1,4,9)-B-[AsW₉V₃O₃₉]⁶⁻ and α -B-[AsW₉O₃₃)₂(VO)₃]⁹⁻ species observed at ca. δ = -544 and -541 ppm, respectively, where the V atoms adopt a square-pyramidal geometry (CN = 5). Consistently, the V nuclei in α -(1,2,3)-[AsW₉V₃O₄₀]⁶⁻ undergo a significant deshielding (δ = -518 ppm), in agreement with their octahedral geometry (CN = 6). The computational ⁵¹V-NMR spectra show a single signal for each of the compounds studied, corresponding to the three vanadium atoms being equivalent by the symmetry of the

molecule. The calculated chemical shift is referred to the VOCl₃ reference using water as the solvent. There is some discrepancy between the absolute values of experimental and calculated shifts, but the general trend is consistently maintained. In addition, the ⁵¹V NMR line width also provides relevant information since the relaxation rate of the quadrupolar nuclei depends on the electric field gradient generated by the surrounding atoms and therefore reflects the symmetry of the coordination sphere of the V nuclei. In this present case, the ⁵¹V NMR line widths of the three compounds lies in a narrow range ($\Delta\nu_{1/2}$ = 240–300 Hz) that makes difficult any qualitative explanation arising from the geometrical environment of the V nuclei. Nevertheless, ⁵¹V NMR in the liquid state could be useful for highlighting protonation processes involving the most basic oxygen atoms of the metal–oxo framework, generally corresponding to those belonging to the first coordination shell of the vanadium centers.^{35,42} Variation of the ⁵¹V NMR chemical shift vs pH is given in Section S7.1. For the α -(1,4,9)-[AsW₉V₃O₃₉]⁶⁻ anion, the plot is consistent with a protonation process featured by a pKa value close to 1, while for the other vanadium Keggin-type anion, α -(1,2,3)-[AsW₉V₃O₄₀]⁶⁻ exhibits a significantly higher value (pKa = 2.25). Such a difference should arise from the specific environment of the three vanadium centers where the μ_3 -oxo group is missing within the {V₃} cap, causing the decrease of the electronic density on the remaining oxo groups.

Furthermore, the ¹⁸³W NMR spectra of the three compounds contain two resonances with a 1:2 intensity ratio for each case, consistent with the C_{3v} local symmetry of the {AsW₉} subunits. However, the ¹⁸³W NMR spectra of both vanadium-containing anions built from the B-type {AsW₉O₃₃} subunits give a similar pattern with a substantial line broadening ($\Delta\nu_{1/2}$ = 30–35 Hz) for the resonance attributed to the six equivalent tungsten atoms due to edge-shared coupling with the ⁵¹V nuclei. Besides, the remaining resonances attributed to the three remaining equivalent W nuclei exhibit a usual line width of 1–2 Hz and gives a very close chemical shift (δ < 1 ppm). Such an observation results from their location far enough from vanadium nuclei. These signals also exhibit a satellite doublet due to ²J_{W-W} coupling of 6 Hz characteristic of the W—O—W edge-shared junctions present in the α -B-{AsW₉O₃₃} subunit (see Section S1), which is significantly different from the ²J_{W-W} coupling value of 17 Hz observed in the α -(1,2,3)-[AsW₉V₃O₄₀]⁶⁻ anion built with W—O—W junctions through shared corners.⁴³ The ¹⁷O NMR spectra of the three species are given in Figure 5c, showing the attributions to the individual oxygen sites. These attributions were established on the basis of experimental⁴⁴ and theoretical⁴⁵ literature data and were supported by the calculations from this study presented in the Section S7.2 and Table S5. As previously observed in the ⁵¹V and ¹⁸³W NMR study, the ¹⁷O NMR spectra of the compounds (1,4,9)-[AsW₉V₃O₃₉]⁶⁻ and [(AsW₉O₃₃)₂(VO)₃]⁹⁻ show similar signatures, but with one notable exception, namely, that the spectrum of the polyanion (1,4,9)-[AsW₉V₃O₃₉]⁶⁻ additionally exhibits a resonance at around 850 ppm. The latter is reasonably attributed to the ¹⁷O nuclei of the V—O_c—V junctions, which do not exist in the compound [(AsW₉O₃₃)₂(VO)₃]⁹⁻. The ¹⁷O NMR spectrum of the Keggin (1,2,3)-[AsW₉V₃O₄₀]⁶⁻ anion shows a resonance associated with the oxygen atoms bridging the vanadium atoms in a region close to that observed for the Keggin B-type ion. Overall, the ¹⁷O NMR spectra of the Keggin ions are very

similar. From a computational point of view, the ^{17}O NMR spectra can help to assign the experimental signals. The agreement between the computed and experimental spectra is very high and reproduces the relative position of the signals with very few differences in ppm. It is noteworthy that the signal corresponding to the V=O oxygen is sensitive to the coordination sphere of the vanadium atom, showing a similar chemical shift of the oxygen bound to the square-pyramidal V, and different to the octahedral case in the A-type. Moreover, the V–O–V oxygen signals are also affected by the coordination of the V atom, with a difference of 90 ppm between the octahedral and square-pyramidal cases. The same behavior is observed in the O signals corresponding to the V–O–W sites. A difference of 80 ppm is observed when comparing the Keggin B-type with the A-type equivalent and 100 ppm with the POM sandwich.

XPS Experiments. X-ray photoelectron spectroscopy (XPS) has been carried out to obtain definitive evidence about the oxidation state of the arsenic ion within the Keggin-type species. For this purpose, both As 3d_{5/2} and As 2p_{3/2} spectral regions were recorded. A photoelectron inelastic mean free path (IMFP) was estimated for the two As-considered peaks according to the TPP2M formula.^{39,40} With an IMFP of 0.6 nm, the As 2p_{3/2} core level probes mainly the upper surface of the material, while the As 3d peak with an IMFP of 2.7 nm is then more representative of the “bulk”. Figure 6a shows the

confirm this trend. While the As 2p_{3/2} signal of the As(V)-containing Keggin-type anion showed, as expected, only a single peak at 1328.1 eV, according to the presence of As(V), those of the As^{III}-containing anion reveal two contributions at 1328.1 and 1326.5 eV, respectively, indicative of the concomitant presence of As^V and As^{III} species.⁴² Since this core level is mostly representative of the top-surface composition, the greater relative proportion of As^V compared to As^{III} highlights the spatial distribution of As atoms. The bulk of this Keggin-type compound is composed of As^{III}, while As^V atoms are located at the surface of the crystals. Since no particular precaution was taken prior to surface analysis, a partial surface oxidation or pollution cannot be excluded in the present case.

Electronic Structure. In addition to the geometric and electronic structure of the α -(1,4,9)-[AsW₉V₃O₃₉]⁶⁻ anion, we also considered the hypothetical P, Sb, and Bi analogues. Their frontier molecular orbital energy levels are pictured in Figure 7. For the P derivative, the HOMO is the heteroatom lone pair orbital (circled) clearly localized in the heteroatom, as depicted in Figure 7. The energy of this lone pair orbital decreases along the series, while the energy of the oxo-band typical in polyoxometalates is hardly affected. Consequently, the HOMO for As, Sb, and Bi is not located in the lone pair orbital anymore but in the orbitals belonging to the oxygen atoms. In all cases, the LUMO orbital corresponds to the fully oxidized vanadium atoms in the cap, i.e., the empty d-band, typical of mixed W–V metal–oxo clusters. Along the series, we observed a slight stabilization of the LUMO level. In all, the smallest HOMO–LUMO gap corresponds to the P species, and the largest to the As system. According to our calculations, although the gap decreases when going from As to Bi, we predict similar stability for the Sb and Bi hypothetical analogues as for the As compound and much smaller for the P derivative. These differences should be observed in the electronic properties.

In addition, several positional isomers could be generated virtually by successive changes of the {AsO₃} orientation in the {W₉V₃O₃₆} oxometallic cage. Such a theoretical study is of interest for assessing the energy cost when the square-pyramidal geometry changes from a vanadium to a tungsten center. Then, four isomers were identified in which the electronic lone pair of the central As(III) atoms was successively directed toward the different types of metallic triads, i.e., {V₃}, {VW₂}, or {W₃} caps as shown in Figure 8a–d. The geometry was optimized for all four isomers, and the Gibbs free energies were calculated and referenced to the first isomer. Results of these calculations showed clearly that the most stable arrangement is obtained when the lone pair is directed toward the three vanadium cap. Changing the {AsO₃} orientation leads to a second isomer with the lone pair pointing toward a {VW₂} triad. Then, the resulting compound contains two W centers and one V center, which adopt a square-pyramidal geometry. Such a change results in a significant decrease of the intrinsic stability, featured by an energy difference close to \sim 13 kcal·mol⁻¹ (see Figure 8). The other two remaining isomers both exhibit in their structure three square-pyramidal W centers in a trimetallic cap. The consequences of these configurations clearly correspond to a large energy increase of \sim 20 kcal·mol⁻¹ for both. These results therefore suggest that the square-pyramidal geometry for W^{VI} atoms is energetically very demanding compared to V^V atoms,

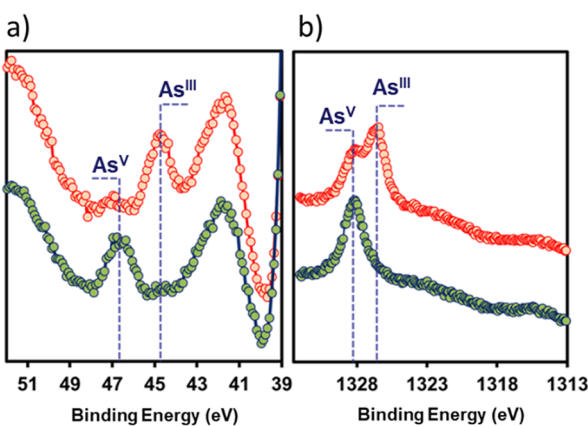


Figure 6. X-ray photoelectron spectra of the α -(1,4,9)-[AsW₉V₃O₃₉]⁶⁻ (red trace) and α -(1,2,3)-[AsW₉V₃O₄₀]⁶⁻ (green trace) anions as potassium salts. (a) Low-energy region highlighting distinctly the As 3d_{5/2} signals characteristic of As^V (46.7 eV) or As^{III} (44.7 eV) within the α -(1,2,3)-[AsW₉V₃O₄₀]⁶⁻ and α -(1,4,9)-[AsW₉V₃O₃₉]⁶⁻ anions, respectively. (b) High-energy region (As 3p_{3/2}) showing the substantial presence of As^V in the top monolayer of the K₆ α -(1,4,9)-[AsW₉V₃O₃₉]⁶⁻ phase. At the same time, the α -(1,2,3)-[AsW₉V₃O₄₀]⁶⁻ species exhibits unambiguously a single peak attributed to the presence of As^V.

XPS signature of the two Keggin-type compounds in the As 3d spectral region. For α -(1,2,3)-[AsW₉V₃O₄₀]⁶⁻ species, the spectrum provides evidence of a single low spin-orbit splitting doublet centered at 46.7 eV, which is characteristic of the As^V oxidation state.⁴¹ Such a situation contrasts significantly with that of the α -(1,4,9)-[AsW₉V₃O₃₉]⁶⁻ species. Even if a weak As^V signal is visible at 46.7 eV, the As 3d_{5/2} spectrum is dominated by a similar doublet but shifted to a lower binding energy (44.7 eV). This energy position is consistent with As atoms at the +III oxidation state.⁴¹ The XPS analyses conducted in the high binding energy domain (Figure 6b)

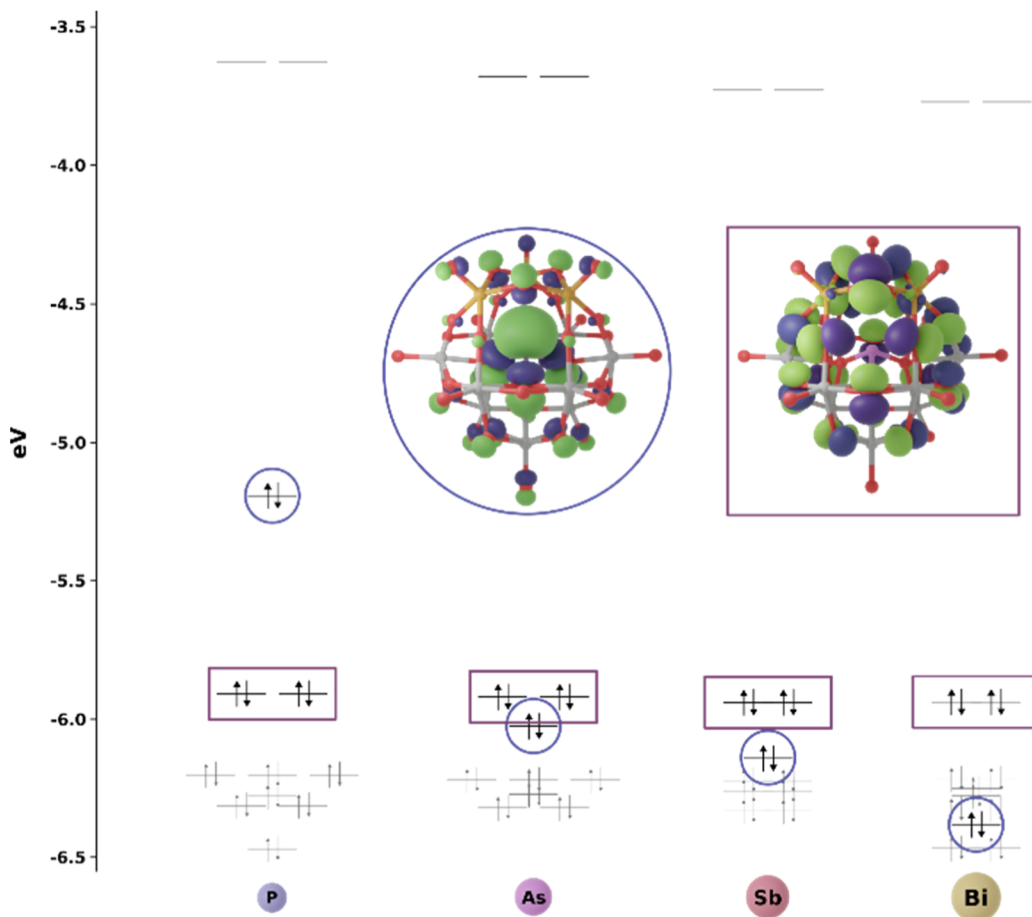


Figure 7. Frontier molecular orbitals' energy levels for the α -(1,4,9)- $[XW_9V_3O_{39}]^{6-}$ ($X = P, As, Sb$, and Bi) anions. Molecular orbital representations for the heteroatom lone pair orbital (circled) and the HOMO for the X derivatives (squared).

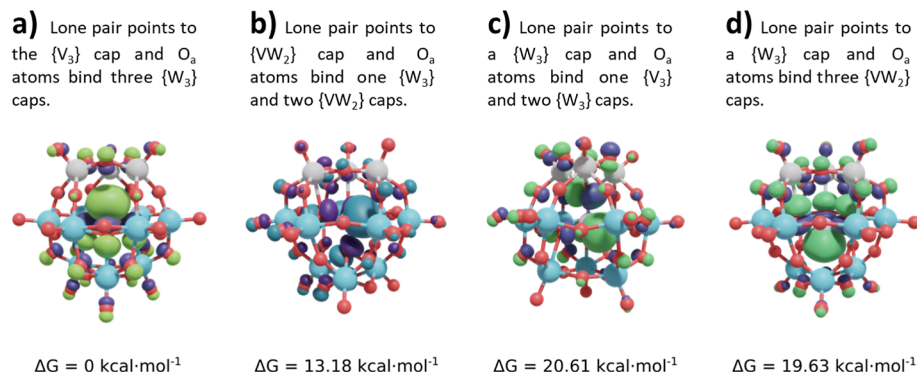


Figure 8. Optimized geometries of the four isomers (labeled (a–d)) corresponding to the different $\{AsO_3\}$ orientation inside the $\{W_9V_3O_{36}\}$ metal–oxo shell. All Gibbs free energies ($\text{kcal}\cdot\text{mol}^{-1}$) are compared to the first isomer ((a) label) where the lone pair orbital of the As^{III} atom points toward the $\{V_3\}$ triad. Color code: red for oxygen, gray for vanadium, light blue for tungsten, and purple for As.

which is in perfect agreement with what was found experimentally.

Electrochemical Behavior and Electronic Spectra. The cyclic voltammograms of the α -(1,4,9)- $[AsW_9V_3O_{39}]^{6-}$ anion have been measured in various buffered aqueous solutions with pH values varying from about 1 to 9. Its CV reveals the typical pattern expected for a three vanadium-containing anion, which should be understood as three successive one-electron transfers (see Figure 9a). While the first electron transfer appears quasi-reversible and nearly pH nondependent ($E^\circ = 0.300 \text{ V vs Ag/AgCl}$, $\Delta P_{a-c} = 60 \text{ mV}$), the two following redox events

corresponding to the formation of the two- and three-electron reduced species appear nearly irreversible featured by two cathodic peaks located at $+0.14$ and $-0.069 \text{ V vs Ag/AgCl}$ and by a single anodic wave at $+0.29 \text{ V vs Ag/AgCl}$. Although it has been established that the redox potentials characterizing electron transfers in POMs depend primarily on the electron charge density, the geometry of the vanadium center also impacts the electronic structure and consequently alters the electrochemical properties. In turn, a nice opportunity is given here to investigate the influence of the square-pyramidal $\{VO_5\}$ versus octahedral $\{VO_6\}$ geometry upon the electron

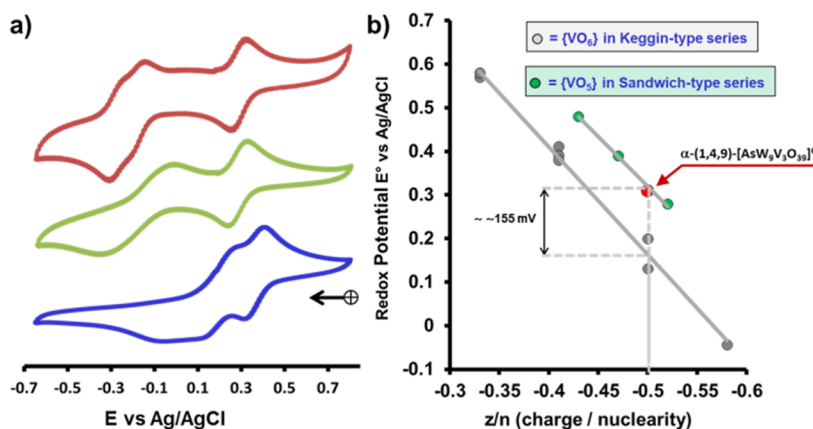


Figure 9. (a) Cyclic voltammograms of the studied vanadium-containing anion $\alpha\text{-(1,4,9)-[AsW}_9\text{V}_3\text{O}_{39}]^{6-}$ collected in an aqueous solution buffered with acetate/acetic acid, pH = 4.75 (blue trace), TRIS/HTRIS, pH = 7.75 (green trace), and NH₃/NH₄Cl, pH = 9.10 (red trace). (b) pH-independent reduction potentials for Keggin anions as a function of z/n parameter with z corresponding to the anion charge and n the metal center nuclearity of the anion. Depending on the geometry of the vanadium center within the Keggin derivatives, two distinct linear correlations are highlighted, revealing that the oxidizing character of the square-pyramidal {VO₅} groups is about 155 mV higher than that of the {VO₆} arrangements.

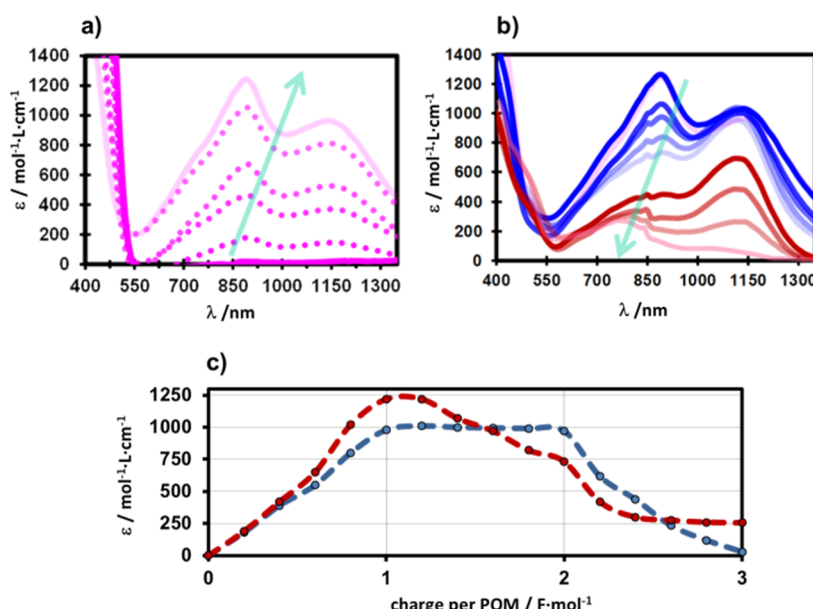


Figure 10. Spectroscopic features in the visible–NIR range of the B-type anion $\alpha\text{-(1,4,9)-[AsW}_9\text{V}_3\text{O}_{39}]^{6-}$ measured in an aqueous solution at pH = 4.75 during the reductive electrolysis experiment: (a) Growth in the IVCTs characterized by $\lambda_{\text{max}} = 1150 \text{ nm (}8700 \text{ cm}^{-1}\text{)} \text{ and } 890 \text{ nm (}11,200 \text{ cm}^{-1}\text{)}$ for n varying from 0 to 1; (b) decrease in IVCTs when the reduction process progresses from 1 up to 3. (c) Variation of the molar absorption coefficient ϵ of IVCT maxima at 1150 nm (red curve) and at 890 nm (blue curve) evidencing three distinct domains separated by the four redox states $n = 0, 1, 2$, and 3.

transfer processes involving the V^V/V^{IV} couple. Therefore, we compared a wide selection of V^V/V^{IV} redox potentials corresponding to the first electron transfer under no protonation condition, involving either an octahedral or a square-pyramidal geometry. Nevertheless, these redox potentials have been plotted against the parameter z/n (see Figure 8b), where z corresponds to the ionic charge fraction and n the metal center nuclearity of the POM species, which corresponds to 12 for the Keggin-type anion or 21 for the sandwich-type species. In fact, this parameter is useful for simply estimating the charge density of the anion, which is necessary to discriminate any contribution from geometry or charge density. Interestingly, graphical representation of E° as a function of z/n shows two distinct and nearly parallel linear

correlations which correspond to {VO₆}-containing Keggin-type series and to the {VO₅} sandwich-type series, respectively. All the details, information, and references concerning the electrochemical data used in Figure 9b are given in Section S8. In addition, it should be noted that our anion $\alpha\text{-(1,4,9)-[AsW}_9\text{V}_3\text{O}_{39}]^{6-}$ belongs fairly to the {VO₅} correlation, in line with the assumed square-pyramidal geometry of its three vanadium centers. Besides, such a graphical representation reveals that {VO₅} centers are intrinsically more oxidant than {VO₆} arrangements. This finding is probably a consequence of the electron density in the vicinity of the V center, which should be higher in {VO₅} than in {VO₆}. Finally, the linear variation in redox potential for the two series of POMs containing vanadium is consistent with the results previously

established by Pope et al.⁴³ Furthermore, the CV of α -(1,4,9)-[AsW₉V₃O₃₉]⁶⁻ reveals additional redox events according to the reduction of the two-remaining vanadium(V) into vanadium(IV) (see Figure 8a). These two one-electron transfers exhibit a weak reversibility at pH lower than 8, while at pH = 9.10, they appear fairly reversible ($\Delta P_{a-c} \sim 60$ mV). This provides evidence that one of the causes of irreversibility probably arises from protonation processes concomitant to the electron transfer which are known to distort the coordination sphere of the vanadium center by lengthening the V–O bond and closing angle of the V–O–V bridge.^{25,44}

Spectroelectrochemistry experiments were also carried out, giving information about the resulting V^V/V^{IV} mixed-valence system. Reduction of the anion was carried out in acetate buffer (pH = 4.7) through electrolysis at a controlled potential carbon electrode (−0.7 V vs Ag–AgCl), allowing the successive reduction of the three vanadium(V) centers into vanadium(IV). The resulting UV-vis spectra in the region above 600 nm are characteristic of the mixed-valence V^V/V^{IV} system (see Figure 10a). As the charge consumed per POM (noted n) increases from 0 to 1, two distinct peaks located at 11,200 cm⁻¹ (890 nm) and 8700 cm⁻¹ (1150 nm) grow continuously, while the electrolysis solution undergoes a color change from orange to green. Attribution of both absorptions is consistent with intervalence charge transfer (IVCTs) V^{IV} → V^V, while those corresponding to V^{IV} → W^{VI} are located in the higher energy range (not shown).⁴⁵ Then, these two absorptions reach their maximum intensity for n = 1. The intensity of the lower energy absorption at 8700 cm⁻¹ remains quite constant ($\epsilon = 1000 \text{ mol}^{-1} \cdot \text{L} \cdot \text{cm}^{-1}$) until n = 2, while that of the other (11,200 cm⁻¹) decreases significantly from 1220 to 730 mol⁻¹·L·cm⁻¹. At last, above n = 2, both absorptions undergo an abrupt decrease of their intensity, in agreement with the expected cancellation of the V^{IV}/V^V IVCTs. As the lower energy absorption gives an intensity close to zero for n = 3, the other undergoes a gradual shift in energy from 11,200 cm⁻¹ (890 nm) to 12,800 cm⁻¹ (780 nm) and reaches a minimum intensity value corresponding to molar absorption coefficient $\epsilon = 260 \text{ mol}^{-1} \cdot \text{L} \cdot \text{cm}^{-1}$ for three V^{IV} ions. It should be noted that this residual absorption is fully consistent in energy (12,800 cm⁻¹) and intensity ($\epsilon = 85 \text{ mol}^{-1} \cdot \text{L} \cdot \text{cm}^{-1}$ per V^{IV} ion) with the contribution of d–d transitions predicted for the {V=O}²⁺ vanadyl species⁴⁶ and previously reported in the literature.³⁴ Besides, variation of the molar extinction coefficient as a function of transferred charge per POM, shown in Figure 10b,c, is fully representative of the three redox states corresponding to 1-, 2-, and 3-electron reduced species.

CONCLUSIONS

In this report, we have summarized experimental and theoretical efforts to provide complementary insights into structural, spectroscopic, and electrochemical properties of a new Keggin B-type anion based on a {AsW₉O₃₃} subunit capped by a vanadium triad {V₃O₆}. Experimental evidence supported by theoretical calculations has unequivocally revealed the nature, location, and geometry of the three vanadium atoms, embedded within the Keggin-type framework. These results showed clearly that changing the geometry of the vanadium atom from octahedral to square pyramidal leads to a significant increase of its oxidant behavior by about 155 mV. This should have important impact for the design of vanadium-based electrodes or composition of vanadium-based

electrolytes involved within redox flow batteries. Moreover, this O-deficient Keggin archetype for mixed metals should not be restricted to this example since polyoxometalate chemistry allows structures containing the typical square-pyramidal environment {O=MO₄}. For instance, niobium(V)-based POMs should be good candidates,^{47,48} but the series could be even extended to molybdenum and tungsten derivatives.²⁸ In this context, our theoretical and experimental research currently being carried out aims to understand the general behavior of these O-deficient Keggin species on the basis of their electronic and physicochemical properties.

EXPERIMENTAL SECTION

Materials and Methods. *Fourier Transform Infrared.* Spectra were recorded on a 6700 Fourier transform infrared (FT-IR) Nicolet spectrophotometer using the diamond ATR technique. The spectra were recorded on nondiluted compounds, and ATR correction was applied.

Raman Spectroscopy. An air-cooled diode laser (LaserOne, 532 nm, 100 mW) was used as the excitation source. Raman experiments were conducted on a custom-delivered Raman probe (SuperHead fiber optic probe, Horiba Scientific), consisting of edge and interference filters for the 532 nm laser, focusing and collecting lens with 55 mm focal length, and two optical fiber connections for the laser and the spectrometer, placed in front of a quartz cuvette containing Keggin-type species dispersed in water. The Raman scattered photons were then analyzed via a spectrometer (iHR-320, 320 mm focal length, Horiba Scientific) coupled with a CCD detector (Syncerity, Horiba Scientific) cooled by the Peltier effect. For all measurements, a Raman laser power of 100 mW, a spectrometer grating of 1800 gr/mm, a slit width of 98 μm, and an exposure time of 5 s were used.

Elemental Analyses. Quantitative analyses of metal contents were carried out by ICP analysis performed in the CREALINS laboratory in Vernaison, France.

Energy-Dispersive X-ray Spectroscopy. EDS measurements were performed using a scanning electron microscope enhanced by a field emission gun equipment (JSM 7001-F, Jeol). The measures were acquired with an SDD XMax 50 mm² detector and the Aztec (Oxford) system working at 15 kV and 10 mm working distance. The quantification is realized with the standard library provided by the constructor using La lines.

Thermogravimetric Analysis (TGA). To determine the water content, a Mettler Toledo thermogravimetric analysis (TGA)/DSC 1, STAR^e System apparatus was used under oxygen flow (50 mL min⁻¹) at a heating rate of 5 °C min⁻¹ up to 700 °C.

Single-Crystal X-ray Diffraction. Intensity data collections were carried out at T = 200(2) K with a Bruker D8 VENTURE diffractometer equipped with a PHOTON 100 CMOS bidimensional detector using high-branching λ μS microfocus X-ray Mo K α monochromatized radiation ($\lambda = 0.71073 \text{ \AA}$). Crystals were glued in paratone oil to prevent any loss of crystallization water. Data reduction was accomplished by using SAINT V7.53a. The substantial redundancy in data allowed a semiempirical absorption correction (SADABS V2.10) to be applied on the basis of multiple measurements of equivalent reflections. Using Olex2,⁴⁹ the structure was solved with the ShelXT⁵⁰ structure solution program using Intrinsic Phasing and refined with the ShelXL refinement package using least-squares minimization. Heavier atoms (W) for each structure were initially located by direct methods. The remaining non-hydrogen atoms were located from Fourier differences and were refined with anisotropic thermal parameters. Thereby, the contribution of solvent–electron density was removed using the SQUEEZE routine in PLATON, producing a set of solvent-free diffraction intensities. Crystallographic data for single-crystal X-ray diffraction studies are summarized, and details about the refinements of the crystal structure are included in Section 4. These data can be obtained free of charge

from The Cambridge Crystallographic Data Centre via <https://www.ccdc.cam.ac.uk/structures-beta/>. Deposit number: 2382113.

Electrochemistry. Deionized water was used throughout the process. It was obtained by passing water through a RiOs 8 unit, followed by a Millipore-Q Academic purification set. All reagents were of high-purity grade and were used as purchased without further purification. Cyclic voltammetric (CV) experiments were carried out with a Metrohm Autolab PGSTAT12 potentiostat/galvanostat associated with a GPES electrochemical analysis system (EcoChemie). Measurements were performed at room temperature in a conventional single-compartment cell. A glassy carbon (GC) electrode with a diameter of 3 mm was used as the working electrode. The auxiliary electrode was a Pt plate placed within a fritted glass isolation chamber, and potentials are quoted against a saturated calomel electrode (SCE). The solutions were deaerated thoroughly for at least 30 min with pure argon and kept under a positive pressure of this gas during the experiments.

NMR (Liquid NMR). All solution NMR spectra were recorded in D₂O at 26 °C. ⁵¹V and ¹⁷O NMR spectra were obtained on a Bruker Avance 400 spectrometer at Larmor frequencies of 105.1 and 54.3 MHz, respectively, by using 5 mm standard NMR tubes. The spectra were recorded with one pulse sequence at 90° flip angle (pulse duration 11 or 20 μ s), using 0.1 s recycle delay, an acquisition time of 80 or 40 ms, and ca. 1000 or 4,000,000 scan numbers, for ⁵¹V and ¹⁷O NMR, respectively. The ¹⁸³W NMR spectra were obtained on a Bruker AVANCE 500 MHz spectrometer using a 10 mm NMR tube, accumulating 32,000 scans of 37 μ s-pulse (90° flip angle) with an acquisition time of 2 s and a relaxation delay of 1 s. Chemical shifts are reported relative to external standards ($\delta = 0$ ppm), 90% VOCl₃ in C₆D₆ for ⁵¹V, H₂O for ¹⁷O, and 1 M Na₂WO₄ aqueous solution for ¹⁸³W.

X-ray Photoelectron Spectroscopy. Few milligrams of material were deposited on a conductive tape for analysis purpose. Regular XPS analyses were conducted on a Thermo Fisher Scientific Nexsa equipped with a monochromated Al K α anode (1486.6 eV) and a dual flood gun (low energy electron and ion). High-energy resolution spectral windows of interest were recorded with a 400 μ m spot size. The photoelectron detection was performed perpendicularly to the surface using a constant analyzer energy (CAE) mode (20 eV pass energy) and a 0.1 eV energy step.

UV–Vis Spectroscopy. UV–vis spectra of solutions were recorded at room temperature on a PerkinElmer Lambda 750 using a calibrated 0.1 cm quartz cell.

Computational Details. The molecular geometries of all polyoxometalates were fully optimized employing the ADF⁵¹ software package (SCM ADF version 2021.101), using the BP86^{52,53} functional, with the relativistic corrections related to the scalar-relativistic zero-order regular approximation (ZORA),^{54,55} using a TZP basis set level. Solvation effects were introduced by means of the continuous solvent model COSMO with Klamt⁵⁶ radii for water. Stationary points were characterized by analytical frequency calculations. All Gibbs free energies were computed at 298.15 K and 1 atm by using the ideal gas-rigid rotor-harmonic oscillator (IGRRHO) model. NMR chemical shifts^{57–59} were computed using the ADF software package (SCM ADF version 2021.101), employing the OPBE⁶⁰ functional and a TZP basis set. Solvation effects were considered using the COSMO model with Klamt radii. A data set collection with all DFT calculations is available in the ioChem-BD⁶¹ repository via the following link 10.19061/iochem-bd-1-338.

Synthesis of the Compounds. The B- and A-type trivacant precursors, i.e., Na₉[α -B–As^{III}W₉O₃₃]·19 H₂O and Na₉[α -A–As^VW₉O₃₄]·18 H₂O, have been synthesized according to reported procedures.^{62–64}

K₆[α -(1,4,9)-As^{III}W₉V^VW₃O₃₉]·14H₂O. Sodium metavanadate (0.74 g; 6.07 mmol) is dissolved in 15 mL of water. The solution is heated at 50 °C, and aqueous acetic acid solution (4 M; 6 mL) is added until the pH drops to 3.4. The solution turned orange. Then, Na₉As^{III}W₉O₃₃·19 H₂O (5 g; 1.90 mmol) was added progressively, leading to a pH increase up to 4.1. The solution is kept under heating and stirring for 1 h. The color turned slightly to red, and the pH

increased until 4.3. The solution was cooled at room temperature, and KCl (3.5 g; 480 mmol) was added under slow stirring, provoking the precipitation of an orange solid. The solution was cooled in ice and stirred slowly for 1 h. The solid was then filtered, washed with EtOH, and dried with Et₂O. The crude orange powder (3.1 g) was redissolved in 20 mL of water. After filtration, the clear resulting solution was allowed to stand for crystallization at room temperature. After 4 days, well-shaped orange crystals (2.4 g) corresponding to K₆AsW₉V₃O₃₉·14 H₂O were collected by filtration and washed with cold water. Yield: 42% (based on W content). Anal. % Calcd. (found): K, 7.8 (7.2); V, 5.1 (5.5); As, 2.5 (2.2); W, 55.3 (55.9); H₂O, 8.4 (8.3).

K₄H₂[α -(1,2,3)-As^VW₉V^VW₃O₄₀]·22H₂O. Sodium metavanadate (1.6 g; 13.11 mmol) is dissolved in 50 mL of water at 50 °C. After complete dissolution, hydrochloric acid aqueous solution (2 M; 2.2 mL) is added slowly until pH drops to 1.5. Then, Na₉[AsW₉O₃₄]·18H₂O (11.4 g; 4.37 mmol) is added into the solution under vigorous stirring. After complete dissolution, the color changes to give an intense red solution, and the pH is readjusted to 1.5 by the addition of an aqueous HCl solution (6 M). After 60 min, successive addition of potassium chloride solid (20 g; 270 mmol) and methanol led to the formation of abundant orange-yellow solid (12–13 g after washing and drying by using ethanol and diethyl ether oxide). This solid is redissolved in 30 mL of distilled water at room temperature. The resulting solution is filtered by using a sintered glass frit to remove insoluble materials. The limpid red solution is cooled by an ice bath, allowing it to stand for crystallization. After 120 min, crystalline solid corresponding to K₄H₂[α -A(1,2,3)-As^VW₉V^VW₃O₄₀]·22H₂O is collected by filtration. Yield: 4 g; 29% based on W. Anal. % Calcd (obs.) for W₉V₃AsK₄H₄₆O₆₂: K, 5.1 (5.4); V, 5.0 (5.3); As, 2.4 (2.2); W, 53.8 (53.4); H₂O, 12.9 (12.6).

ASSOCIATED CONTENT

Data Availability Statement

A data set collection with all DFT calculations is available in the ioChem-BD repository⁶¹ via the following link 10.19061/iochem-bd-1-338.

Supporting Information

The Supporting Information is available free of charge at <https://pubs.acs.org/doi/10.1021/acs.inorgchem.5c00637>.

Additional experimental details, materials, and methods, including computational details, IUPAC numbering, X-ray diffraction analysis and refinement, structural representations, vibrational spectroscopies (experimental and theoretical), multinuclear liquid NMR (pKa's determination and calculated NMR chemical shifts), and electrochemical analysis (PDF)

Accession Codes

Deposition Number 2382113 contains the supplementary crystallographic data for this paper. These data can be obtained free of charge via the joint Cambridge Crystallographic Data Centre (CCDC) and Fachinformationszentrum Karlsruhe Access Structures service.

AUTHOR INFORMATION

Corresponding Authors

Mohamed Haouas – Institut Lavoisier de Versailles, UMR 8180 CNRS, UVSQ, Université Paris-Saclay, 78035 Versailles, France; orcid.org/0000-0002-2133-702X; Email: mohamed.haouas@uvsq.fr

Carles Bo – Institute of Chemical Research of Catalonia (ICIQ), The Barcelona Institute of Science and Technology, 43007 Tarragona, Spain; orcid.org/0000-0001-9581-2922; Email: cbo@iciq.cat

Emmanuel Cadot — Institut Lavoisier de Versailles, UMR 8180 CNRS, UVSQ, Université Paris-Saclay, 78035 Versailles, France; orcid.org/0000-0003-4136-6298; Email: emmanuel.cadot@uvsq.fr

Authors

Fa Ibrahima Bamba — Institut Lavoisier de Versailles, UMR 8180 CNRS, UVSQ, Université Paris-Saclay, 78035 Versailles, France

Clément Falaise — Institut Lavoisier de Versailles, UMR 8180 CNRS, UVSQ, Université Paris-Saclay, 78035 Versailles, France; orcid.org/0000-0003-2000-3113

Nathalie Leclerc — Institut Lavoisier de Versailles, UMR 8180 CNRS, UVSQ, Université Paris-Saclay, 78035 Versailles, France

Gildas Gbassi — UFR Sciences Pharmaceutiques et Biologiques (UFR SPB), Université Félix Houphouet Boigny (UFHB), BP V34 Abidjan, Côte d'Ivoire

Patrick Athéba — UFR Sciences des Structures de la Matière et Technologie (UFR SSMT), Université Félix Houphouet Boigny (UFHB), BP V34 Abidjan, Côte d'Ivoire

Mathieu Fregnaux — Institut Lavoisier de Versailles, UMR 8180 CNRS, UVSQ, Université Paris-Saclay, 78035 Versailles, France; orcid.org/0000-0002-3915-3982

Jordi Buils — Institute of Chemical Research of Catalonia (ICIQ), The Barcelona Institute of Science and Technology, 43007 Tarragona, Spain; Departament de Química Física I Inorgànica, Universitat Rovira I Virgili, 43007 Tarragona, Spain

Mireia Segado-Centellas — Departament de Química Física I Inorgànica, Universitat Rovira I Virgili, 43007 Tarragona, Spain

Complete contact information is available at:

<https://pubs.acs.org/10.1021/acs.inorgchem.5c00637>

Author Contributions

Fa Ibrahima Bamba, experimental tasks such as synthesis of the compounds, electrochemistry, NMR, TGA, IR-FT, and ICP elemental analysis. **Clément Falaise**, experimental studies and related analyses, including single-crystal X-ray structure analysis, electrochemistry, UV-vis, Raman and infrared spectroscopies, and contribution to the writing of the manuscript. **Nathalie Leclerc**, supervision of the experimental tasks including chemical synthesis, electrochemistry, and thermal and elemental analyses. **Mohamed Haouas**, supervision of the liquid NMR investigations, analysis of the multinuclear NMR data, and contribution to writing of the manuscript. **Gildas Gbassi** supervisor and project management. **Patrick Athéba**, general supervision of the experimental tasks. **Mathieu Fregnaux**, XPS and Raman studies and contribution to the writing of the manuscript. **Jordi Buils**, computational calculations such as electronic structure studies and IR, Raman and NMR calculations, and contribution to the writing of the manuscript. **Mireia Segado-Centellas**, supervision of the computational tasks. **Carles Bo**, writing of the manuscript and project management (lead). **Emmanuel Cadot**, writing of the manuscript and project management (lead).

Notes

The authors declare no competing financial interest.

ACKNOWLEDGMENTS

This work is supported by a public grant overseen by the French National Research Agency as part of the “Investissements d’Avenir” program (Labex Charm3at, ANR-11-LABX-0039-grat) and by the Paris Ile-de-France region-DIM “Respose”. The Ivory Coast Government is acknowledged for the F-I-B doctoral grant. The CNRS (France) and the University of Versailles Saint Quentin (UVSQ, France) are also acknowledged for financial support. We acknowledge the Spanish Ministry of Science, Innovation and Universities MCIN/AEI/10.13039/501100011033 (PID2020-112806RB-I00 and CEX2019-000925-S), the ICIQ Foundation, and the CERCA program of the Generalitat de Catalunya for funding.

REFERENCES

- (1) Pope, M. T. *Heteropoly and Isopoly Oxometalates*; Springer-Verlag: Berlin and Heidelberg: Berlin, 1983.
- (2) Pope, M. T.; Müller, A. Polyoxometalate Chemistry: An Old Field with New Dimensions in Several Disciplines. *Angew. Chem., Int. Ed.* **1991**, *30* (1), 34–48.
- (3) Gumerova, N. I.; Rompel, A. Polyoxometalates in Solution: Speciation under Spotlight. *Chem. Soc. Rev.* **2020**, *49* (21), 7568–7601.
- (4) Launay, J. P. Réduction de l’ion métatungstate: Stades éléves de réduction de $[H_2W_{12}O_{40}]^{6-}$, dérivés de $[HW_{12}O_{40}]^{7-}$ et discussion générale. *J. Inorg. Nucl. Chem.* **1976**, *38*, 807–816.
- (5) Chen, J.-J.; Symes, M. D.; Cronin, L. Highly Reduced and Protonated Aqueous Solutions of $[P_2W_{18}O_{62}]^{6-}$ for on-Demand Hydrogen Generation and Energy Storage. *Nat. Chem.* **2018**, *10* (10), 1042–1047.
- (6) Wang, H.; Hamanaka, S.; Nishimoto, Y.; Irle, S.; Yokoyama, T.; Yoshikawa, H.; Awaga, K. In Operando X-Ray Absorption Fine Structure Studies of Polyoxometalate Molecular Cluster Batteries: Polyoxometalates as Electron Sponges. *J. Am. Chem. Soc.* **2012**, *134* (10), 4918–4924.
- (7) Lee, J.-S.; Lee, C.; Lee, J.-Y.; Ryu, J.; Ryu, W.-H. Polyoxometalate as a Nature-Inspired Bifunctional Catalyst for Lithium–Oxygen Batteries. *ACS Catal.* **2018**, *8* (8), 7213–7221.
- (8) Robin, M. B.; Day, P. Mixed Valence Chemistry-A Survey and Classification. *Adv. Inorg. Chem. Radiochem.* **1968**, *10*, 247–422.
- (9) Jordan, J. W.; Lowe, G. A.; McSweeney, R. L.; Stoppiello, C. T.; Lodge, R. W.; Skowron, S. T.; Biskupek, J.; Rance, G. A.; Kaiser, U.; Walsh, D. A.; Newton, G. N.; Khlobystov, A. N. Host–Guest Hybrid Redox Materials Self-Assembled from Polyoxometalates and Single-Walled Carbon Nanotubes. *Adv. Mater.* **2019**, *31* (41), 1904182.
- (10) Hu, J.; Diao, H.; Luo, W.; Song, Y.-F. Dawson-Type Polyoxomolybdate Anions ($P_2Mo_{18}O_{62}^{6-}$) Captured by Ionic Liquid on Graphene Oxide as High-Capacity Anode Material for Lithium-Ion Batteries. *Chem.–Eur. J.* **2017**, *23* (36), 8729–8735.
- (11) Xiao, C.; Zhang, L.; Wang, K.; Wang, H.; Zhou, Y.; Wang, W. A New Approach to Enhance Photocatalytic Nitrogen Fixation Performance via Phosphate-Bridge: A Case Study of SiW12/K-C3N4. *Appl. Catal., B* **2018**, *239*, 260–267.
- (12) Zhou, X.; Yu, H.; Zhao, D.; Wang, X.; Zheng, S. Combination of Polyoxotantalate and Metal Sulfide: A New-Type Noble-Metal-Free Binary Photocatalyst $Na_8Ta_6O_{19}/Cd_{0.7}Zn_{0.3}S$ for Highly Efficient Visible-Light-Driven H_2 Evolution. *Appl. Catal., B* **2019**, *248*, 423–429.
- (13) Simms, C.; Kondinski, A.; Parac-Vogt, T. N. Metal-Addenda Substitution in Plenary Polyoxometalates and in Their Modular Transition Metal Analogues. *Eur. J. Inorg. Chem.* **2020**, *2020* (27), 2559–2572.
- (14) Lv, H.; Guo, W.; Wu, K.; Chen, Z.; Bacsa, J.; Musaev, D. G.; Geletii, Y. V.; Lauinger, S. M.; Lian, T.; Hill, C. L. A Noble-Metal-Free, Tetra-Nickel Polyoxotungstate Catalyst for Efficient Photocatalytic Hydrogen Evolution. *J. Am. Chem. Soc.* **2014**, *136* (40), 14015–14018.

- (15) Tourneur, J.; Fabre, B.; Loget, G.; Vacher, A.; Mériadec, C.; Ababou-Girard, S.; Gouttefangeas, F.; Joanny, L.; Cadot, E.; Haouas, M.; Leclerc-Laronze, N.; Falaise, C.; Guillou, E. Molecular and Material Engineering of Photocathodes Derivatized with Polyoxometalate-Supported {Mo₃S₄} HER Catalysts. *J. Am. Chem. Soc.* **2019**, *141* (30), 11954–11962.
- (16) Benseghir, Y.; Solé-Daura, A.; Mialane, P.; Marrot, J.; Dalecky, L.; Béchu, S.; Frégnaux, M.; Gomez-Mingot, M.; Fontecave, M.; Mellot-Draznieks, C.; Dolbecq, A. Understanding the Photocatalytic Reduction of CO₂ with Heterometallic Molybdenum(V) Phosphate Polyoxometalates in Aqueous Media. *ACS Catal.* **2022**, *12* (1), 453–464.
- (17) Nagaiah, T. C.; Gupta, D.; Adhikary, S. D.; Kafle, A.; Mandal, D. Tuning Polyoxometalate Composites with Carbonaceous Materials towards Oxygen Bifunctional Activity. *J. Mater. Chem. A* **2021**, *9* (14), 9228–9237.
- (18) Li, X.-H.; He, P.; Wang, T.; Zhang, X.-W.; Chen, W.-L.; Li, Y.-G. Keggin-Type Polyoxometalate-Based ZIF-67 for Enhanced Photocatalytic Nitrogen Fixation. *ChemSusChem* **2020**, *13* (10), 2769–2778.
- (19) Bonchio, M.; Syrgiannis, Z.; Burian, M.; Marino, N.; Pizzolato, E.; Dirian, K.; Rigodanza, F.; Volpato, G. A.; La Ganga, G.; Demitri, N.; Berardi, S.; Amenitsch, H.; Guldi, D. M.; Caramori, S.; Bignozzi, C. A.; Sartorel, A.; Prato, M. Hierarchical Organization of Perylene Bisimides and Polyoxometalates for Photo-Assisted Water Oxidation. *Nat. Chem.* **2019**, *11* (2), 146–153.
- (20) Toma, F. M.; Sartorel, A.; Iurlo, M.; Carraro, M.; Parisse, P.; Maccato, C.; Rapino, S.; Gonzalez, B. R.; Amenitsch, H.; Da Ros, T.; Casalis, L.; Goldoni, A.; Marcaccio, M.; Scorrano, G.; Scoles, G.; Paolucci, F.; Prato, M.; Bonchio, M. Efficient Water Oxidation at Carbon Nanotube–Polyoxometalate Electrocatalytic Interfaces. *Nat. Chem.* **2010**, *2* (10), 826–831.
- (21) Zhong, J.; Pérez-Ramírez, J.; Yan, N. Biomass Valorisation over Polyoxometalate-Based Catalysts. *Green Chem.* **2021**, *23* (1), 18–36.
- (22) Zha, B.; Li, C.; Li, J. Efficient Electrochemical Reduction of CO₂ into Formate and Acetate in Polyoxometalate Catholyte with Indium Catalyst. *J. Catal.* **2020**, *382*, 69–76.
- (23) Meyer, R. L.; Anjass, M. H.; Petel, B. E.; Brennessel, W. W.; Streb, C.; Matson, E. M. Electronic Consequences of Ligand Substitution at Heterometal Centers in Polyoxovanadium Clusters: Controlling the Redox Properties through Heterometal Coordination Number. *Chem.—Eur. J.* **2020**, *26* (44), 9905–9914.
- (24) Tommasino, J. B.; Contant, R.; Michaut, J. P.; Roncin, J. Electrochemical Characterization of a Series of Substituted Dawson Type Tungstophosphates $\alpha[P_2W_{18-x}Mo_xV_yO_{62}]^{n-}$ ($x = y + z$; $n = 6 + y$). *Polyhedron* **1998**, *17* (2), 357–366.
- (25) Cadot, E.; Thouvenot, R.; Teze, A.; Herve, G. Syntheses and Multinuclear NMR Characterizations of α -[SiMo₂W₉O₃₉]⁸⁻ and Alpha-[SiMo_{3-x}V_xW₉O₄₀]^{(4+x)-} ($x = 1, 2$) Heteropolyoxometalates. *Inorg. Chem.* **1992**, *31* (20), 4128–4133.
- (26) Abbessi, M.; Contant, R.; Thouvenot, R.; Hervé, G. Dawson Type Heteropolyanions. 1. Multinuclear (Phosphorus-31, Vanadium-51, Tungsten-183) NMR Structural Investigations of Octadeca-(Molybdotungstovanado)Diphosphates α -1,2,3-[P₂MM'W₁₅O₆₂]ⁿ⁻ ($M, M' = Mo, V, W$): Syntheses of New Related Compounds. *Inorg. Chem.* **1991**, *30* (8), 1695–1702.
- (27) Contant, R.; Abbessi, M.; Thouvenot, R.; Hervé, G. Dawson Type Heteropolyanions. 3. Syntheses and 31P, 51V, and 183W NMR Structural Investigation of Octadeca(Molybdo–tungsto–vanado)–Diphosphates Related to the [H₂P₂W₁₂O₄₈]¹²⁻ Anion. *Inorg. Chem.* **2004**, *43* (12), 3597–3604.
- (28) Jeannin, Y.; Martin-Frere, J. Tungsten-183 NMR and x-Ray Study of a Heteropolyanion [As₂W₂₁O₆₉(H₂O)]⁶⁻ Exhibiting a Rare Square-Pyramidal Environment for Some Tungsten(VI). *J. Am. Chem. Soc.* **1981**, *103* (7), 1664–1667.
- (29) Robert, F.; Leyrie, M.; Herve, G.; Teze, A.; Jeannin, Y. Crystal-Structure of Ammonium Dicobalto(II)-40-Tungstotetraarsenate(III) - Allosteric Effects in the Ligand. *Inorg. Chem.* **1980**, *19* (6), 1746–1752.
- (30) Leyrie, M.; Thouvenot, R.; Teze, A.; Herve, G. Polyoxotungstates with Lone-Pair Assembling Atoms. I: Alkali and Alkaline Earth Cryptates of the [Co₂(H₂O)₂ As₄W₄₀O₁₄₀]²⁴⁻ Inorganic Complex. Interaction Between the Metal Centers. *New J. Chem.* **1987**, *16* (4), 475–481.
- (31) Kortz, U.; Savelieff, M. G.; Bassil, B. S.; Dickman, M. H. A Large, Novel Polyoxotungstate: [As₆W₆₅O₂₁₇(H₂O)₇]²⁶⁻. *Angew. Chem., Int. Ed.* **2001**, *40* (18), 3384–3386.
- (32) Lefebvre, F.; Leyrie, M.; Herve, G.; Sanchez, C.; Livage, J. Square Pyramidal Complexes of Divalent Cations of the First Transition Row with the 20-Tungsto-2-Arsenate(III): Synthesis, Visible and E.S.R. Spectra. *Inorg. Chim. Acta* **1983**, *73*, 173–178.
- (33) Lin, Z.; Izarova, N. V.; Mehari, F. T.; Kortz, U. Palladium(II) Incorporation in the All-Inorganic Cryptand [As₄W₄₀O₁₄₀]²⁸⁻: Synthesis and Structural Characterization of [Pd₂Na₂KAs₄W₄₀O₁₄₀(H₂O)₂]²¹⁻. *Z. Anorg. Allg. Chem.* **2018**, *644* (22), 1379–1382.
- (34) Bamba, I. F.; Falaise, C.; Marrot, J.; Gbassi, G. K.; Atheba, P.; Guillot, R.; Haouas, M.; Cadot, E. Revisiting the Three Vanadium Sandwich-Type Polyoxometalates: Structures, Solution Behavior, and Redox Properties. *Inorg. Chem.* **2022**, *61* (21), 8309–8319.
- (35) Leparulo-Loftus, M. A.; Pope, M. T. Vanadium-51 NMR Spectroscopy of Tungstovanadate Polyanions. Chemical Shift and Line-Width Patterns for the Identification of Stereoisomers. *Inorg. Chem.* **1987**, *26* (13), 2112–2120.
- (36) Domaille, P. J.; Watunya, G. Synthesis and Tungsten-183 NMR Characterization of Vanadium-Substituted Polyoxometalates Based on B-Type Tungstophosphate PW₉O₃₄⁹⁻ Precursors. *Inorg. Chem.* **1986**, *25* (8), 1239–1242.
- (37) Jeannin, Y. P. The Nomenclature of Polyoxometalates: How To Connect a Name and a Structure. *Chem. Rev.* **1998**, *98* (1), 51–76.
- (38) Sundaram, K. M.; Neiwert, W. A.; Hill, C. L.; Weinstock, I. A. Relative Energies of α and β Isomers of Keggin Dodecatungstogallate. *Inorg. Chem.* **2006**, *45* (3), 958–960.
- (39) Tanuma, S.; Powell, C. J.; Penn, D. R. Calculations of Electron Inelastic Mean Free Paths. V. Data for 14 Organic Compounds over the 50–2000 eV Range. *Surf. Interface Anal.* **1994**, *21* (3), 165–176.
- (40) Shinotsuka, H.; Tanuma, S.; Powell, C. J.; Penn, D. R. Calculations of Electron Inelastic Mean Free Paths. X. Data for 41 Elemental Solids over the 50 eV to 200 keV Range with the Relativistic Full Penn Algorithm. *Surf. Interface Anal.* **2015**, *47* (9), 871–888.
- (41) Mizokawa, Y.; Iwasaki, H.; Nishitani, R.; Nakamura, S. Esca Studies of Ga, As, GaAs, Ga₂O₃, As₂O₃ and As₂O₅. *J. Electron Spectrosc. Relat. Phenom.* **1978**, *14* (2), 129–141.
- (42) Rei Vilar, M.; El Beghdadi, J.; Debontridder, F.; Artzi, R.; Naaman, R.; Ferraria, A. M.; Botelho do Rego, A. M. Characterization of Wet-Etched GaAs (100) Surfaces. *Surf. Interface Anal.* **2005**, *37* (8), 673–682.
- (43) Altenau, J. J.; Pope, M. T.; Prados, R. A.; So, H. Models for Heteropoly Blues. Degrees of Valence Trapping in Vanadium(IV)- and Molybdenum(V)-Substituted Keggin Anions. *Inorg. Chem.* **1975**, *14* (2), 417–421.
- (44) Mossoba, M. M.; O'Connor, C. J.; Pope, M. T.; Sinn, E.; Herve, G.; Teze, A. Mixed Valence and Magnetically Coupled Vanadate Domains in Heteropoly Tungstate Anions. *J. Am. Chem. Soc.* **1980**, *102* (22), 6864–6866.
- (45) Harmalker, S. P.; Leparulo, M. A.; Pope, M. T. Mixed-Valence Chemistry of Adjacent Vanadium Centers in Heteropolytungstate Anions. I. Synthesis and Electronic Structures of Mono-, Di-, and Trisubstituted Derivatives of Alpha-Octadecatungstodiphosphate(6-) Ion (α -[P₂W₁₈O₆₂]⁶⁻). *J. Am. Chem. Soc.* **1983**, *105* (13), 4286–4292.
- (46) Ballhausen, C. J.; Gray, H. B. The Electronic Structure of the Vanadyl Ion. *Inorg. Chem.* **1962**, *1* (1), 111–122.
- (47) Son, J.-H.; Casey, W. H. Reversible Capping/Uncapping of Phosphorous-Centered Keggin-Type Polyoxonobate Clusters. *Chem. Commun.* **2015**, *51* (8), 1436–1438.
- (48) Shmakova, A. A.; Abramov, P. A.; Sokolov, M. N. Synthesis, Stability, and Crystal Structure of the

(NMe₂H₂)₉[{(AsW₉O₃₃)₂(NbO)₃(H₂O)]·44H₂O Complex. *J. Struct. Chem.* **2019**, *60* (4), 623–629.

(49) Dolomanov, O. V.; Bourhis, L. J.; Gildea, R. J.; Howard, J. a. K.; Puschmann, H. OLEX2: a complete structure solution, refinement and analysis program. *J. Appl. Crystallogr.* **2009**, *42*, 339–341.

(50) Sheldrick, G. M. SHELXT – Integrated space-group and crystal-structure determination. *Acta Crystallogr., Sect. A:Found. Adv.* **2015**, *71*, 3–8.

(51) Te Velde, G.; Bickelhaupt, F. M.; Baerends, E. J.; Fonseca Guerra, C.; Van Gisbergen, S. J. A.; Snijders, J. G.; Ziegler, T. Chemistry with ADF. *J. Comput. Chem.* **2001**, *22* (9), 931–967.

(52) Becke, A. D. Density-Functional Exchange-Energy Approximation with Correct Asymptotic Behavior. *Phys. Rev. A* **1988**, *38* (6), 3098–3100.

(53) Perdew, J. P. Density-Functional Approximation for the Correlation Energy of the Inhomogeneous Electron Gas. *Phys. Rev. B* **1986**, *33* (12), 8822–8824.

(54) Van Lenthe, E.; Baerends, E. J. Optimized Slater-type Basis Sets for the Elements 1–118. *J. Comput. Chem.* **2003**, *24* (9), 1142–1156.

(55) Lenthe, E. V.; Baerends, E. J.; Snijders, J. G. Relativistic Regular Two-Component Hamiltonians. *J. Chem. Phys.* **1993**, *99* (6), 4597–4610.

(56) Klamt, A. Conductor-like Screening Model for Real Solvents: A New Approach to the Quantitative Calculation of Solvation Phenomena. *J. Phys. Chem.* **1995**, *99* (7), 2224–2235.

(57) Autschbach, J.; Ziegler, T. Nuclear Spin–Spin Coupling Constants from Regular Approximate Relativistic Density Functional Calculations. II. Spin–Orbit Coupling Effects and Anisotropies. *J. Chem. Phys.* **2000**, *113* (21), 9410–9418.

(58) Autschbach, J.; Ziegler, T. Nuclear Spin–Spin Coupling Constants from Regular Approximate Relativistic Density Functional Calculations. I. Formalism and Scalar Relativistic Results for Heavy Metal Compounds. *J. Chem. Phys.* **2000**, *113* (3), 936–947.

(59) Schreckenbach, G.; Ziegler, T. Calculation of NMR Shielding Tensors Using Gauge- Including Atomic Orbitals and Modern Density Functional Theory. *J. Phys. Chem.* **1995**, *99* (2), 606–611.

(60) Swart, M.; Ehlers, A. W.; Lammertsma, K. Performance of the OPBE Exchange-Correlation Functional. *Mol. Phys.* **2004**, *102* (23–24), 2467–2474.

(61) Alvarez-Moreno, M.; De Graaf, C.; López, N.; Maseras, F.; Poblet, J. M.; Bo, C. Managing the Computational Chemistry Big Data Problem: The ioChem-BD Platform. *J. Chem. Inf. Model.* **2015**, *55* (1), 95–103.

(62) Robert, F.; Leyrie, M.; Hervé, G. Structure of potassium diaquaticcuprocatadecatungstodiarsenate(III)(12-) undecahydrate. *Acta Crystallogr., Sect. B* **1982**, *38*, 358–362.

(63) Tourne, C.; Tourne, G. 19-Tungstodimetallo-Diarsenates 3 Preliminary Study. *C. R. Hebd. Séances Acad. Sci., Ser. C* **1975**, *281* (22), 933–936.

(64) Contant, R.; Thouvenot, R.; Dromzée, Y.; Proust, A.; Gouzerh, P. Synthesis and Structural Chemistry of Tungstoarsenates(V). *J. Cluster Sci.* **2006**, *17* (2), 317–333.